



Silver incorporated into cryptomelane-type Manganese oxide boosts the catalytic oxidation of benzene



Hua Deng^a, Shunyu Kang^{a,b}, Jinzhu Ma^{a,b,c,*}, Changbin Zhang^{b,c}, Hong He^{a,b,c}

^a Center for Excellence in Regional Atmospheric Environment, Key Laboratory of Urban Pollutant Conversion, Institute of Urban Environment, Chinese Academy of Sciences, Xiamen, 361021, China

^b University of Chinese Academy of Sciences, Beijing, 100049, China

^c State Key Joint Laboratory of Environment Simulation and Pollution Control, Research Center for Eco-Environmental Sciences, Chinese Academy of Sciences, Beijing, 100085, China

ARTICLE INFO

Keywords:

Manganese oxide
Cryptomelane
Silver
Volatile organic compounds
Catalytic oxidation
XAFS

ABSTRACT

Different amounts of silver were successfully incorporated into cryptomelane-type manganese oxide (K-OMS-2) via a one-step hydrothermal method for application in the catalytic combustion of benzene. Silver incorporation could promote the benzene oxidation performance of the catalysts. The silver doping effect was addressed in terms of the relationship between structure and activity. The prepared catalysts were characterized by ICP-OES, BET, XRD, Raman, FE-SEM, TEM, XPS, XAFS, H₂-TPR and CO-TPD. The best precursor Mn/Ag mole ratio was 40. The resulting K/Ag-OMS-40 catalyst exhibited the highest activity in terms of benzene combustion and good tolerance to chlorine poisoning, all of which make it a promising candidate as an alternative to noble metal supported catalysts. All catalysts after silver incorporation maintained the structural integrity of the cryptomelane structure but with decreased crystalline size, which significantly increased the surface area and number of defects of the catalyst. The silver species, mostly in the form of Ag⁺, were well dispersed and partially replaced K⁺ in the tunnels of cryptomelane. K/Ag-OMS-40 had the largest surface area, the smallest nanorods and most abundant Mn octahedral defects. The large number of active oxygen species derived from the high Mn³⁺ content and Ag-O-Mn bridge bonds appeared to play critical roles in VOC decomposition.

1. Introduction

Volatile organic compounds (VOCs) emitted from many industrial processes and transportation activities are one of the major contributors to air pollution [1–5]. The catalytic destruction of VOCs is an important pollutant control issue, and the noble metal (Pd and/or Pt) catalysts are recognized as some of the most desirable candidates [6–9]. However, due to their low natural abundances and high costs, the search for economical catalysts as alternatives to noble metal catalysts has drawn more and more interest.

The inexpensive and environmentally friendly cryptomelane-type octahedral molecular sieve (K-OMS-2, formula KMn₈O₁₆·nH₂O) [10,11] is a promising catalyst for the catalytic oxidation of VOCs. For instance, Li et al. [12,13] have demonstrated good reactivity for ethanol and acetaldehyde over OMS-2. Benzyl alcohol [14,15], ethyl acetate [16], o-xylene [17,18], toluene [19] and trichloroethylene [20] also have been reported to be effectively degraded over OMS-2 catalysts. K-OMS-2 is

composed of corner- and edge-shared MnO₆ octahedra, forming a 2 × 2 tunnel structure with K⁺ ions inside the tunnel. Suib et al. [21–25] have reported that the structure, morphology, valence of manganese species, and lattice parameters of OMS-2 can be easily tuned and that a very strong size/structure property functionality relationship has been established. Li et al. [26,27] and Yu et al. [28] have summarized progress in the field and proposed several useful strategies: (1) Morphology control; by selecting a suitable synthesis method or parameters, the morphology of OMS-2 can be controlled to be nanorods, nanowires, or nanofibers [29]. With the change in morphology, a high amount of active surface may be exposed, leading to an enhancement in catalytic performance. (2) Multiple substitution of transition metal ions into the cryptomelane OMS-2 structure. This is the most common way to modify the redox activity of OMS-2, and further to increase its catalytic properties [30]. To date, a number of metals ions have been used such as Ti [31], V [32], Fe [33], Co [34], Cu [34,35], W [24], Ce [26,34,36]. (3) Ion-exchange of K⁺ in the channels of OMS-2. Exchanging K⁺ by Li⁺,

* Corresponding author at: Center for Excellence in Regional Atmospheric Environment, Key Laboratory of Urban Pollutant Conversion, Institute of Urban Environment, Chinese Academy of Sciences, Xiamen, 361021, China.

E-mail address: jzma@rcees.ac.cn (J. Ma).

Cs^+ etc. [37] causes enhancement of the reducibility and framework basicity of OMS-2. Recently, tuning the concentration of K^+ in the tunnels of OMS-2 was found to be one of the most efficient approaches for enhancing the performance in VOC abatement [27]. Catalytic oxidation over OMS-2 usually proceeds via the Mars-van Krevelen mechanism [26,27,30,37–39]. Organic molecules adsorbed on the catalyst surface are oxidized by labile surface oxygen, and the resultant oxygen vacancies are subsequently replenished by gas-phase O_2 . Thus, promoting the surface oxygen reactivity is critical. It is well-known that silver (Ag) can adsorb and activate gaseous O_2 [40,41], and silver can also exchange for K^+ in the tunnels of K-OMS-2, both which are thought to be effective means to tune the catalytic oxidation efficiency of the catalyst toward VOCs.

To the best of our knowledge, the effects of doping concentration on Ag location in K-OMS-2 and the resultant impacts on textural properties, morphology, and reactivity of oxygen species have not been fully investigated. Consequently, this study was undertaken to advance the current knowledge on the relationship between structure and activity for K/Ag-OMS-2. The catalytic oxidation of benzene was used as a model reaction [42] to help screen catalysts. Besides, carcinogenic and recalcitrant benzene also has been regarded as a priority hazardous substance in need of elimination. K/Ag-OMS-2 catalysts were synthesized by a facile one-step hydrothermal method. The location of Ag within K-OMS-2 at different doping levels was determined by various characterization techniques. The catalytic performance of Ag/K-OMS-2 for benzene removal was fully investigated. The resultant impacts on the textural properties, morphology, and reactivity of oxygen species were revealed.

2. Materials and methods

2.1. Experimental section

The K-OMS-2 materials were prepared by reaction between a Mn^{2+} salt precursor and potassium permanganate via a hydrothermal method as in our previous reports [43,44]. On the basis of our preliminary experiments, the precursor Mn/Ag mole ratio of 40 was found to be most favorable to prepare good catalysts. Since the doping concentration of Ag could influence the Ag location in K-OMS-2 and the resultant textural properties, the effect of changes in the Ag concentration was addressed in this study. During the synthesis of silver-incorporated K-OMS-2, different silver loadings (with precursor Mn/Ag mole ratio of 80, 40, 20 respectively) were prepared by mixing an appropriate amount of AgNO_3 with the Mn^{2+} precursor first. The detailed procedure was as follows: an appropriate amount of AgNO_3 mixed with 18.34 g of $\text{MnAc}_2 \cdot 4\text{H}_2\text{O}$ was dissolved in deionized water under stirring. 12.5 mL glacial acetic acid was then added in order to form an acidic environment. Next a solution of 10.84 g KMnO_4 in deionized water was added slowly to the above mixture under stirring. Finally, the mixed solution was maintained at 100 °C for 24 h in a 500 mL Teflon-lined autoclave and then cooled to room temperature. The resulting black slurry was centrifuged, washed with deionized water and dried at 100 °C overnight. Then the sample was calcined in a furnace at 500 °C for 3 h. The final samples were denoted as K/Ag-OMS-x. For example, a sample denoted as K/Ag-OMS-40 means Ag incorporated in K-OMS-2 with the precursor Mn/Ag mole ratio of 40.

2.2. Catalytic measurements

The catalytic combustion tests for benzene were conducted in a fixed bed continuous flow quartz reactor (8 mm i.d.) at temperatures from 150 to 400 °C. The temperature programming procedures were: heating at a rate of 2.5 °C/min or 5 °C/min to each measurement temperature followed by stabilizing for 50 min. The sampling frequency was five times for each measurement temperature, with the average values given. About 0.2 g of catalyst was used for each experiment. The

gas flow passing through the reactor was C_6H_6 (1500 ppm), CH_2Cl_2 (400 ppm, when used), water vapor (5%, when used), and O_2 (20%) in N_2 balance at 300 mL/min. The GHSV value was 45,000 h^{-1} ($\text{SV} = 90,000 \text{ mL h}^{-1} \text{ g}^{-1}$). The benzene concentration was analyzed online by a gas chromatograph (GC; Agilent 7890B, HP-5 capillary column) with flame ionization detector. CO_2 and O_2 concentrations were analyzed by the same GC equipped with a thermal conductivity detector (Porapak Q and HayeSep Q column). In all the experiments, C_6H_6 conversion was calculated using the following equation:

$$\text{C}_6\text{H}_6 \text{ Conversion (\%)} = (1 - \frac{[\text{C}_6\text{H}_6]_{\text{out}}}{[\text{C}_6\text{H}_6]_{\text{in}}}) \times 100\%$$

The CO_2 yield was defined as follows:

$$\text{CO}_2 \text{ Yield (\%)} = \frac{[\text{CO}_2]_{\text{out}}}{[\text{C}_6\text{H}_6]_{\text{in}} \times 6} \times 100\%$$

2.3. Catalyst characterization

Nitrogen adsorption-desorption isotherms were measured using a Quantachrome QuadraSorb evo system at 77 K. The specific surface area of the samples was calculated by the Brunauer-Emmett-Teller (BET) method. The volume of pores was determined by the Barrett-Joyner-Halenda (BJH) method from the desorption branches of the isotherms.

The X-ray powder diffraction patterns of the various catalysts were collected on a wide angle X'Pert Pro XRD diffractometer (PANalytical B.V., Netherlands), using $\text{CuK}\alpha$ radiation ($\lambda = 1.5406 \text{ \AA}$) at 40 kV and 40 mA with a scanning speed of 5°/min. The patterns were taken over the 20 range from 10° to 90°.

Raman spectra were recorded on a laser Raman spectrometer (LabRAM Aramis, HORIBA Jobin Yvon, France) and excitation was provided by an He-Ne laser (633 nm), with 8 scans per spectrum and 2 cm^{-1} resolution.

X-ray photoelectron spectroscopy (XPS) measurements were carried out with an ESCALAB250 spectrometer using a monochromated Al $\text{K}\alpha$ X-ray source (1486.6 eV). The binding energy was calibrated using the adventitious C 1 s peak at 284.6 eV. The continuum spectrum was fitted according to Gaussian-Lorentzian line shapes.

Elemental analysis was conducted using an inductively coupled plasma emission spectrometer (ICP-OES, Optima 7000DV). All samples were dissolved using strong acid solution before being tested. The calibration solution was prepared using pure standards.

The morphology of catalysts was imaged using a Hitachi S-4800 scanning electronic microscope (Hitachi, Japan). High resolution transmission electron microscopy (HRTEM) was performed on a JEOL JEM-ARM2100 F TEM with a Cs-corrected probe operated at 200 kV.

The XANES and EXAFS of Mn-K edges were measured in transmission mode at room temperature on the BL14W1beam line, Shanghai Synchrotron Radiation Facility (SSRF), Shanghai China. Before measurements, all samples were crushed and sieved to 200 mesh or finer and then diluted with flour powder at appropriate ratios and pressed into thin disks.

The samples (60 mg) loaded in a quartz reactor were pretreated at 300 °C in a flow of 20 vol.% O_2/Ar (50 mL/min) for 0.5 h and cooled down to room temperature (30 °C) followed by Ar purging for 0.5 h. Then a 50 mL/min gas flow of 10% H_2 in Ar was passed over the samples through a cold trap to the detector. The reduction temperature was linearly raised at 5 °C min^{-1} from 30 to 600 °C.

The temperature-programmed desorption of CO (CO-TPD) measurements on the samples were carried out on a laboratory-built fixed-bed instrument with a temperature-programmed furnace. The catalysts were loaded in a quartz reactor and heated at 300 °C for 1 h in 100 mL/min He flow. After being cooled to ambient temperature, the samples were saturated by 1 vol% CO/He mixed gas for 1 h. Then the flow gas was changed to pure He for 0.5 h, followed by temperature ramping to

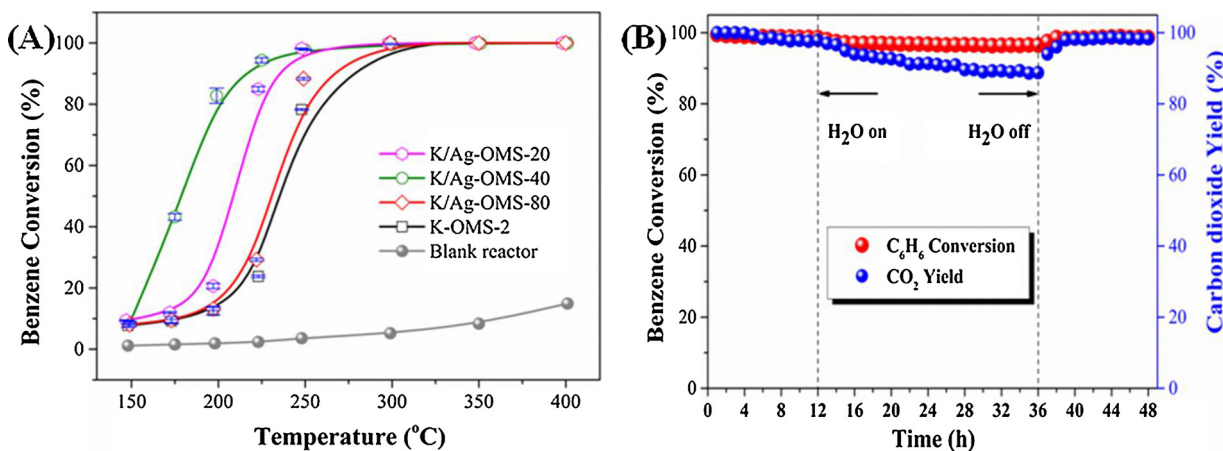


Fig. 1. (A) C_6H_6 conversion over different K/Ag-OMS-x catalysts, (B) Stability test of K/Ag-OMS-40 catalyst in terms of C_6H_6 conversion and CO_2 yield at a temperature of 250 °C.

500 °C at a linear rate of 10 °C min⁻¹. The products CO and CO₂ were monitored using an Ametek LC-D200 M PRO Mass Spectrometer at m/z ratios of 28 and 44, respectively.

3. Results and discussion

3.1. Catalytic activity of K/Ag-OMS-x catalyst

The conversion of C_6H_6 over different catalysts is displayed in Fig. 1. It can be clearly seen in Fig. 1(A) that the silver loading effect was profound. Increasing the silver loading (synthetic Mn/Ag ratio ranging from 80:1 to 40:1) significantly enhanced the C_6H_6 conversion. Further increasing the silver loading (as Mn/Ag = 20:1) substantially decreased the C_6H_6 conversion. The sample K/Ag-OMS-40 exhibited the highest C_6H_6 conversion, so a stability test was performed for this sample. It is clearly shown in Fig. 1(B) that the catalyst exhibited excellent stability, maintaining nearly 100% C_6H_6 conversion and CO_2 yield at the temperature of 250 °C for a 12 h test. Adding 5 vol% H₂O into the gas feed, the C_6H_6 conversion was depressed to a certain extent. The catalyst could also maintain above 98% C_6H_6 conversion and 90% CO_2 yield throughout another 24 h test. Switching off the moisture, K/Ag-OMS-40 regained almost complete mineralization of benzene.

The sample K/Ag-OMS-40 was also compared with a noble metal catalyst (1 wt% Pd/Al₂O₃) as shown in Fig. 2. K/Ag-OMS-40 clearly exhibited C_6H_6 conversion very close to that of Pd/Al₂O₃. Li et al. [27] have reported that tuning the K⁺ concentration in the tunnel of OMS-2

can be used to obtain low-cost and environmentally benign candidates to substitute for 0.5% Pt/Al₂O₃ under SV = 48,000 mLg⁻¹ h⁻¹. Tang et al. [40] have demonstrated that Ag₁/HMO catalysts (T50 is 170 °C) exhibit marginally better activity than Pt/Al₂O₃ or Pd/Al₂O₃ under GHSV of 23,000 h⁻¹. Our catalysts exhibited outstanding combined performance in terms of catalytic efficiency, GHSV value (this study 45,000 h⁻¹ / 90,000 mLg⁻¹ h⁻¹) and low cost compared to catalysts reported in the literature. Moreover, the chlorine tolerance of K/Ag-OMS-40 and Pd/Al₂O₃ were compared by addition of 400 ppm dichloromethane (DCM) in the flow. As clearly shown in Fig. 2(A), introduction of DCM significantly depressed the activity of both catalysts. However, K/Ag-OMS-40 exhibited much better tolerance to chlorine poisoning than Pd/Al₂O₃. The tolerance difference between the K/Ag-OMS-40 and Pd/Al₂O₃ catalysts was also evaluated by stability testing. Both catalysts exhibited excellent stability, maintaining nearly 100% C_6H_6 conversion at the temperature of 300 °C in a flow of benzene and air. However, when 400 ppm CH₂Cl₂ (DCM) was added into the gas feed, the C_6H_6 conversion was depressed to 80% and 20% of the original values for K/Ag-OMS-40 and Pd/Al₂O₃ respectively. After adding 5 vol% H₂O into the DCM-containing gas feed, the C_6H_6 conversion for both catalysts increased marginally. Switching off the DCM and moisture, both catalysts regained over 90% conversion of benzene. All the above results demonstrated that the K/Ag-OMS-40 is an effective candidate for application in elimination of volatile organic compounds. A synergistic effect derived from silver and cryptomelane enhanced the catalytic performance.

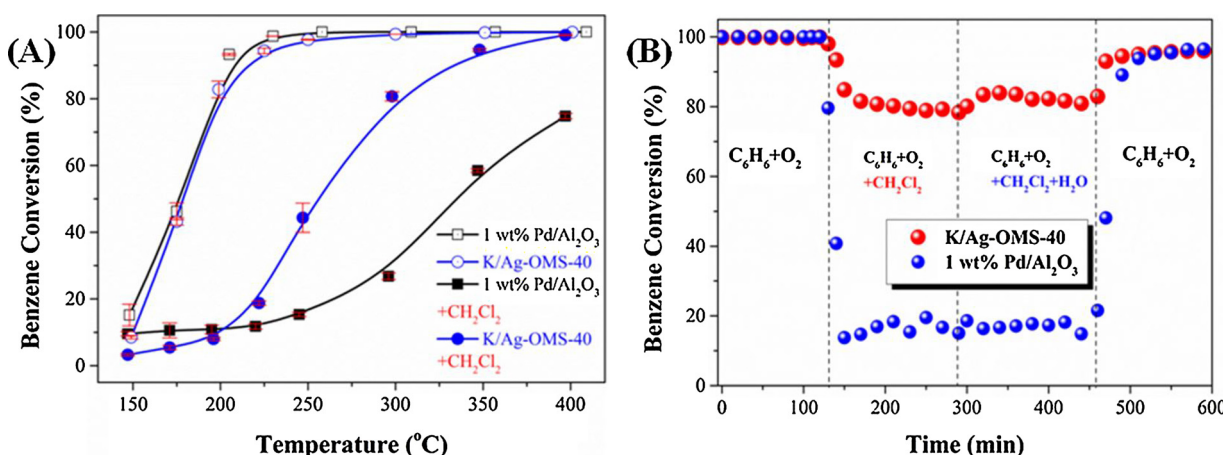


Fig. 2. (A) Comparison of C_6H_6 conversion between K/Ag-OMS-40 (GHSV = 45,000 h⁻¹) and 1 wt% Pd/Al₂O₃ (GHSV = 40,000 h⁻¹). (B) Stability test of K/Ag-OMS-40 and 1 wt% Pd/Al₂O₃ catalyst in terms of chlorine and moisture tolerance at temperature of 300 °C.

Table 1

Textural parameters of all catalysts derived from N₂ physisorption results and the contents of K, Mn and Ag metals determined by ICP-OES.

Sample	BET (m ² /g)	Pore volume (ml/g)	Micropores (ml/g, m ² /g)	Mesopores (ml/g, m ² /g)	K (K/Mn) (wt%)	(wt%)	Mn (wt%)
K-OMS-2-fresh	79.6	0.80	—	—	5.5 (0.141)	—	55.7
K-OMS-2	59.3	0.25	(0.01, 2.9)	(0.13, 10.2)	5.2 (0.139)	—	55.9
K/Ag-OMS-80	75.5	0.54	(0.00, 0.0)	(0.33, 23.2)	5.0 (0.127)	1.3 (0.012)	55.6
K/Ag-OMS-40	133.2	0.51	(0.01, 1.2)	(0.46, 67.7)	3.8 (0.099)	2.7 (0.025)	55.2
K/Ag-OMS-20	105.3	0.57	(0.01, 7.7)	(0.49, 51.0)	3.9 (0.105)	2.8 (0.026)	53.7

3.2. Structural properties

The surface areas and pore volume values of K-OMS-2 and K/Ag-OMS-x catalysts, including micropores and mesopores, are listed in **Table 1**. The N₂ isotherms and cumulative surface areas as a function of pore width are illustrated in Fig. S1(A) and (B) respectively. Thermal calcination caused the surface area of K-OMS-2 to decline to 59.3 m²/g, which is close to values in other reports [11,13,27,28,35,40,43,44]. Although the cryptomelane-type manganese oxides have a pore opening of about 0.46 nm according to the crystal structure, the effective pore opening may be in the range of about 0.265–0.333 nm since charge balancing ions like K⁺ block the pores [45–48]. Therefore, it is hard for molecular N₂ (0.33 nm) [47,48] or C₆H₆ (0.55 nm) [40] molecules to enter into the micropores. The pore-size distribution curves are plotted in **Fig. 3(A)**, which unambiguously demonstrate that the micropores are negligible and can be ruled out in oxidizing benzene. After silver loading, the surface areas of K/Ag-OMS-x were gradually increased, which can be attributed to the gradually enhanced mesopore structure as shown in **Fig. 3(A)** and **Table 1**. The surface area of K/Ag-OMS-40 was the highest among all Mn-related samples at 133.2 m²/g,

but still lower than the counterpart of 1 wt% Pd/Al₂O₃, with 198.3 m²/g (Fig. S2). We can tentatively assume that enhanced mesopores derived from the silver substitution increase the surface area and adsorption sites for VOCs, which is favorable for the decomposition of benzene vapor.

XRD patterns of the four catalysts are shown in **Fig. 3(B)**. The four samples exhibited similar diffraction patterns. The (110), (200), (310), (211), (301), (411), (600), (521), (002), (541), (730) reflections at 2θ values of 12.7, 18.0, 28.7, 37.4, 41.8, 50.0, 55.3, 60.0, 65.3, 69.8, and 72.3 degrees, respectively, match the pattern of synthetic cryptomelane (KMn₈O₁₆, ICDD No. 00-29-1020) [10,11,13,15,21,27,28,35,43]. No additional peaks assignable to compounds of silver species appear in these materials, confirming that the silver species are well dispersed and probably incorporated into the OMS-2 channels. However, the characteristic diffraction peaks are broadened and decreased in intensity when the precursor Mn/Ag ratio is below 40. This indicates that Ag addition causes the formation of a poorly crystalline phase or a decrease in the crystal size.

The lattice structure of catalysts was investigated by Raman spectroscopy as shown in **Fig. 3(C)**. Pristine K-OMS-2 exhibits four distinct

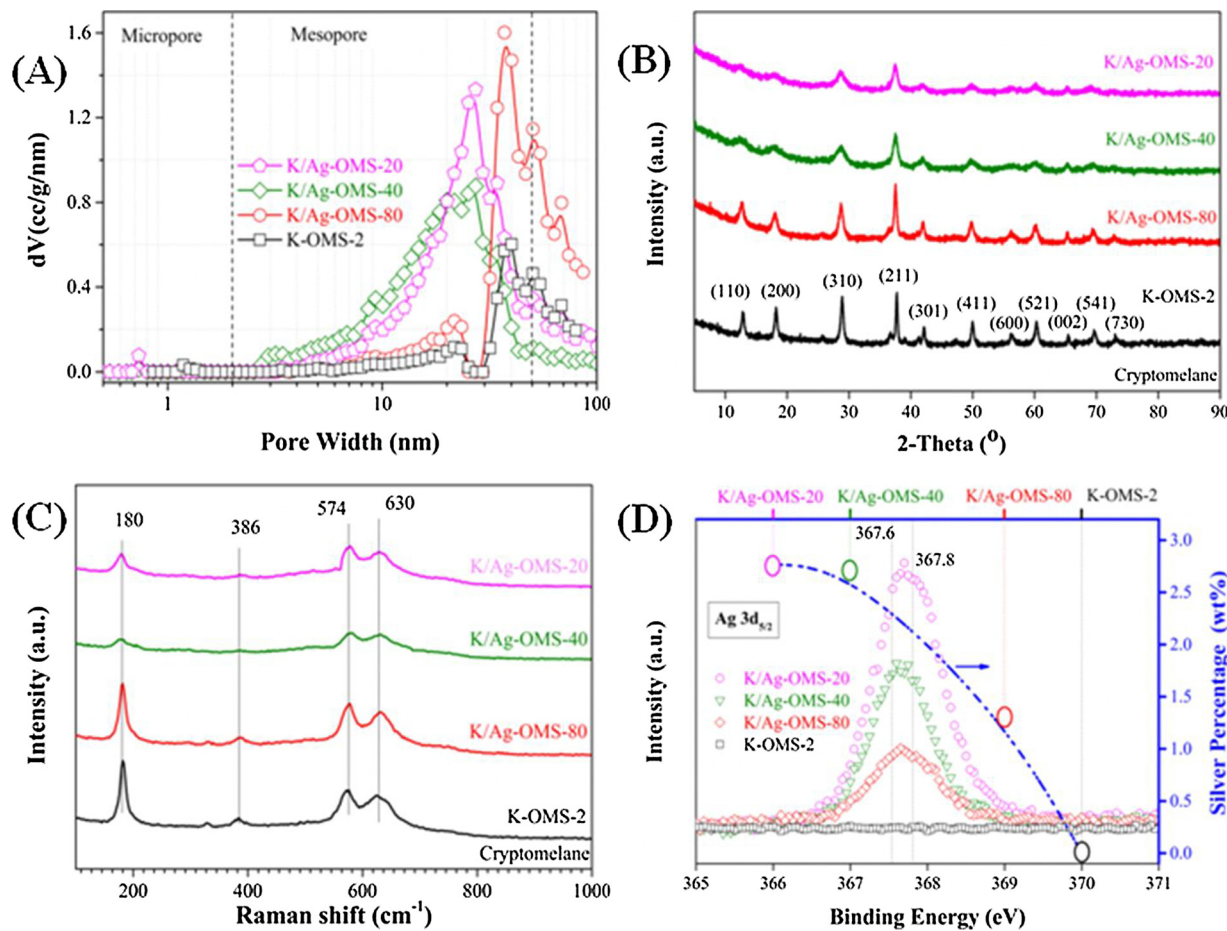


Fig. 3. (A) Pore-size distribution (B) XRD spectra, (C) Raman spectra, (D) Ag 3d XPS spectra and bulk silver amount for the series of K/Ag-OMS-x catalysts.

Raman peaks. The peaks at 180 and 386 cm⁻¹ can be ascribed to the deformation modes of Mn-O-Mn, while the peaks at 574 and 630 cm⁻¹ can be assigned to the Mn-O vibrations that are along and orthogonal to the direction of the MnO₆ octahedral double chains respectively [13,24,35,44,49]. With the increase of Ag doping level, K/Ag-OMS-x samples show Raman spectral characteristics similar to those of pristine K-OMS-2, but the spectra become weaker and broader. This is a size-dependent phenomenon commonly observed with nanoparticles [50], which reveals that the particle size of the samples decreases. This observation is consistent with the BET and XRD results and also agrees with the reports of Li et al. [49] and Ma et al. [44]. Since the Raman peak assigned to the Mn—O bond did not red- or blue-shift after silver loading, the Mn—O bond strength can be ruled out as having a key role in benzene oxidation in this case.

In order to confirm the position of the silver in the structure, the bulk contents of K, Mn and Ag for all the catalysts were determined by ICP-OES and presented in Table 1. The K amount in K-OMS-2 is marginally larger than the ideal content of cryptomelane (with K/Mn mole ratio of 0.125) due to excessive K from the KMnO₄ source during synthesis. Therefore, the tunnel of cryptomelane should be saturated by K⁺. The bulk Mn mass ratios (wt%) for K/Ag-OMS-80 and K/Ag-OMS-40 were close to that of the pure K-OMS-2 catalyst, implying that the main cryptomelane structure is preserved after silver loading. More importantly, the bulk K mass ratio decreased with the increase of silver incorporation loading. On the basis of the above results, we can conclude that silver introduced in the synthesis mixture caused partial replacement of potassium ions in the tunnels [51,52].

The XPS binding energies of Ag 3d_{5/2} for all K/Ag-OMS-x samples are in the range of 367.6–367.8 eV, as shown in Fig. 3(D), which could be attributed to the characteristics of Ag⁺ [47,48,53]. Silver species in the OMS-2 structure are mostly Ag⁺ and are well dispersed in the micropores [54,55]. According to Dyer and co-workers [56], manganese oxides are very effective for selective adsorption of Ag⁺ in strongly acidic solution, even in the presence of large amounts of other cations such as K⁺, Cs⁺, and Sr²⁺. As for K/Ag-OMS-40, the bulk Mn/Ag mole ratio is equal to the precursor Mn/Ag ratio, suggesting that all of the initially added silver has been incorporated into the cryptomelane channels. Presumably, the MnO₆ octahedra are simultaneously arranged around potassium and/or silver as template ions during the formation of cryptomelane. However, as the precursor Mn/Ag ratio decreases to 20, the selectivity of Ag⁺ over K⁺ is no longer observed since the bulk Ag amount reaches a plateau, as shown in Fig. 3(D). The excess silver may be excluded by the MnO₆ units, implying that the structure of OMS-2 has limited Ag uptake capacity. It is generally accepted that K⁺ ions (0.28 nm) are located in the channels of the OMS-2 structure in order to balance the charge in the structure [21–25]. The replacement of K⁺ by Ag⁺, with the smaller radius of 0.24 nm [53], may result in the tunnel becoming distorted. The slight distortion of the unit cell may induce more lattice defects, which are thought to be beneficial for catalytic oxidation performance.

The nanostructure of the products was examined with FESEM, TEM and HRTEM (Figs. S3 and S4). All of the produced materials display a needle-like fibrous morphology, typical of OMS-2 materials [21–25,27,28,35,43,44]. The average nanorod length for K-OMS-2 is 173 nm, while that for K/Ag-OMS-80 decreased to 145 nm, as shown in Fig. 4. On increasing the silver doping, the fiber lengths decrease to the lowest value of 39 nm for K/Ag-OMS-40. On the contrary, on further increasing the precursor silver content, the length is increased to 72 nm. For ease of comparison, the nanostructures of K-OMS-2 and K/Ag-OMS-40 are displayed in Fig. 5(A) and (B). Consistent with the BET, XRD and Raman results, partial exchange of tunnel K⁺ by Ag⁺ during the one-step synthesis of K-OMS-2 impedes the generation of long cryptomelane nano-rods, as illustrated in Figs. 4 and 5. The HRTEM images shown in Fig. 5(C) and (D) reveal that the sample exhibits well-defined lattice fringes. The width of neighboring lattice fringes is 0.47–0.49 nm, corresponding to the diffraction pattern of the (200) zone axis of tetragonal

cryptomelane-type MnO₂ [10,21–23,29,57]. The lattice structure agreed well with the above XRD and Raman results, confirming that the crystalline structure of cryptomelane is preserved even after extensive silver loading, but the size of nanorods is substantially decreased after silver loading. As depicted in Fig. 5, no silver particles can be found and the overlapping of Mn, O and Ag element mapping demonstrates that silver is homogeneously dispersed in the preserved cryptomelane structure, all of which confirms that silver ions are well dispersed in the tunnels of K-OMS-2.

3.3. Local structure and chemical state of Mn octahedra

As stated above, the silver species are well dispersed in the tunnels of cryptomelane. The benzene molecule (0.55 nm) cannot gain access to the Ag⁺ ions due to steric hindrance. Thus, silver incorporation should indirectly influence the Mn octahedral structure and finally boost the benzene oxidation, which is quite different from the behavior of Ag/HMO, with isolated Ag atoms serving as the active sites [40]. In order to learn the local structure of K-OMS-2 after partial silver exchange into the tunnel, the X-ray absorption fine structure of the Mn-K edge, including XANES and EXAFS, was measured using Mn foil, MnO, Mn₂O₃, and α-MnO₂ as reference materials. Fig. 6 shows the filtered k³-weighted EXAFS oscillations Fourier transformed into R space of the Mn K-edge in the series of K-OMS-2 and K/Ag-OMS-x catalysts. The single and multiple scattering paths from the tetragonal cryptomelane structure (space group I4/m) of α-MnO₂ were used as the reference model. [43,44,49] Good curve fitting degrees could be obtained (Fig. S5), and the curve fitted data are presented in Table 2.

As shown in Fig. 6(A) and (B), a bond distance at 1.90 Å was observed for all samples, which can be assigned to a Mn-O shell. A peak at ca. 2.90 Å could be assignable to backscattering from the Mn-Mn₁ shell. The peak at ca. 3.40 Å could be ascribed to the Mn-Mn₂ shell. It is clear that silver doping significantly decreased the coordination number in the Mn-Mn₁ and Mn-Mn₂ shells, indicating that more abundant crystalline defects are formed involving Mn octahedra. Among samples with different silver loadings, K/Ag-OMS-40 has both the lowest coordination number for the Mn-Mn coordination shell and the best benzene decomposition performance. These results unambiguously reveal that the crystalline defects involving Mn octahedra play a critical role in the catalytic performance in eliminating VOCs. Mn cation vacancies are influential in the catalytic activity due to the creation of coordinatively unsaturated oxygens that are excellent sites for proton binding [11], and decomposition of hydrocarbons should be enhanced via proton abstraction. In brief, the synergistic effect of silver incorporation into cryptomelane can be attributed to Ag⁺ incorporated in the cryptomelane tunnel, maintaining the crystalline structural integrity but decreasing the particle size, which causes an explosion in the surface area and number of Mn octahedral defects.

Manganese in octahedral coordination is mainly present as Mn⁴⁺ and Mn³⁺ [10,11,21–25,43,44,58]. The mixed valence (Mn⁴⁺ and Mn³⁺) in K-OMS-2 catalysts is important for electron transport, because the efficiencies of catalysts are usually governed by their ability and tendency to cycle between different valence states of the relevant metal ions [25,59]. In order to understand the effect of silver incorporation on the chemical state of the Mn skeleton in K/Ag-OMS-x, the average oxidation state (AOS) of manganese was calculated first. The XPS of Mn 3s is best suited for verifying the manganese oxidation state [60], therefore the XPS of Mn 3s were investigated and the results are illustrated in Fig. S6. The AOS of all samples were estimated to range from 3.75 to 3.87. In other words, Mn⁴⁺ is dominant (accounting for 87% of total Mn) in the pristine K-OMS-2 structure ($K_1^{+} Mn_1^{3+} Mn_7^{4+} O_{16}$, $Mn^{4+}/(Mn^{3+} + Mn^{4+}) = 87.5\%$) [11,24,57]. The content of Mn³⁺ increases by about 10% after silver doping, since the AOS decreases to 3.75 (Mn⁴⁺ accounting for 75% of total Mn).

In order to discern the subtle differences in mixed-valence manganese among K/Ag-OMS-x samples, Mn-K XANES of samples with

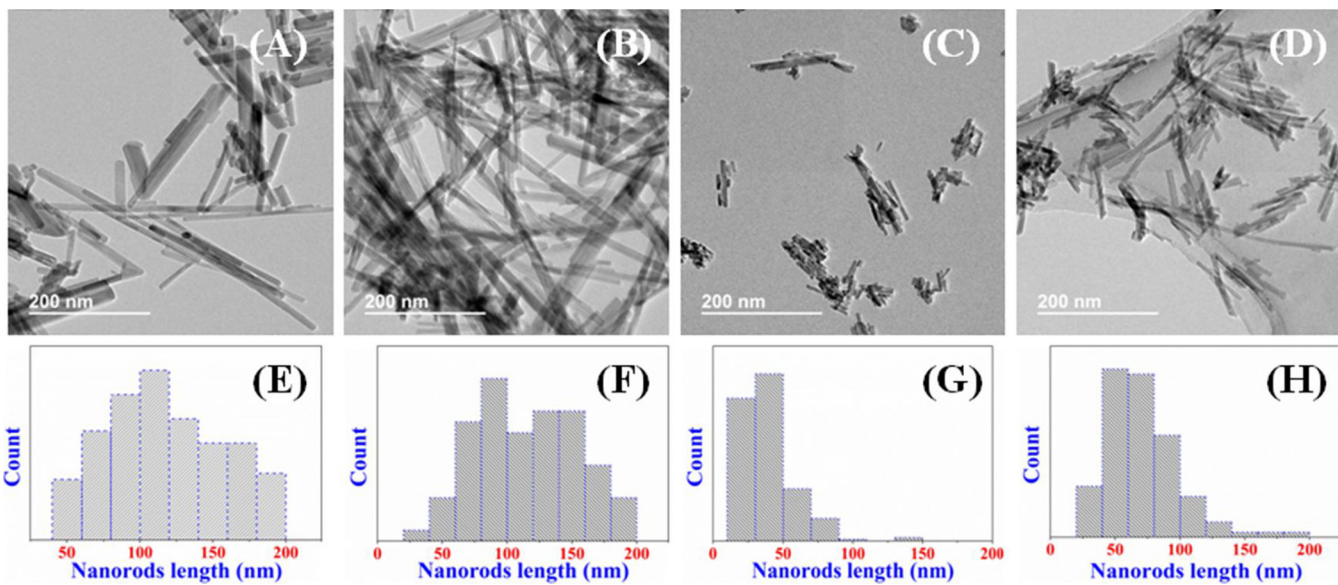


Fig. 4. TEM/nanorod length distribution of K/Ag-OMS-x catalysts: K-OMS-2 (A and E), K/Ag-OMS-80 (B and F), K/Ag-OMS-40 (C and G), K/Ag -OMS-20 (D and H).

different silver loadings were compared to the spectra of MnO , Mn_2O_3 and Mn_2O_5 reference materials (Fig. S7). The Ag-OMS-x catalysts show similar XANES spectra to those of K-Mn $_{2-}$ O $_2$ and Mn $_{2-}$ O $_3$. The increment (ΔM) of Mn $^{3+}$ in K/Ag-OMS-x catalysts calculated by the Rex2000 analysis package was 1.9%, 7.5%, and 4.7% for K/Ag-OMS-80, K/Ag-OMS-40 and K/Ag-OMS-20, respectively. Linear combination fitting of the XANES spectra is exhibited in Fig. 6(C), which demonstrates that K/Ag-OMS-40 exhibits the most abundant Mn $^{3+}$. Exchange of tunnel K $^+$ by Ag $^+$ could give rise to more Mn $^{3+}$ formation, because the replacement of K $^+$ by the smaller radius Ag $^+$ ion results in the structure of K-OMS-2 becoming distorted. TEM and HRTEM results, as shown in Fig. 4, confirmed that the average nanorod size decreased after silver incorporation and can be ranked as follows: K-OMS-2 (173 nm) > K/Ag-OMS-80 (145 nm) > K/Ag-OMS-20 (72 nm) > K/Ag-OMS-40 (39 nm). As for the local structures, the Mn octahedral defects increase in order of K-OMS-2 < K/Ag-OMS-80 < K/Ag-OMS-20 < K/Ag-OMS-40 as depicted in Fig. 6(A), which is negatively correlated with the nanorod length. On the other hand, the increment (ΔM) of Mn $^{3+}$ in K/Ag-OMS-x varies as follows: K-OMS-2 < K/Ag-OMS-80 < K/Ag-OMS-

20 < K/Ag-OMS-40, as illustrated in Fig. 6(C). The Mn $^{3+}$ formation is clearly consistent with the formation of Mn octahedral defects. In fact, more abundant Mn octahedral defects/Mn $^{3+}$ are formed after silver incorporation, and K/Ag-OMS-40 exhibited the most abundant Mn octahedral defects and highest Mn $^{3+}$ content.

The increase of Mn $^{3+}$ in the K-OMS-2 nanorod samples suggests that more oxygen vacancies are generated: $-\text{Mn}^{4+}-\text{O}^{2-}-\text{Mn}^{4+}-\rightarrow-\text{Mn}^{3+}-\square-\text{Mn}^{3+}- + 1/2\text{O}_2$ [11,24,27,49,57,61]. Li et al. [27] has proved that increasing the oxygen vacancy concentration can improve the lattice oxygen activity. On the other hand, silver exchange can form new Ag-O-Mn interaction entities, which could also accelerate the charge transfer along Ag-O-Mn bridges [62,40,52,53]. For instance, the Ag $^+$ cation in Ag-OMS-2 may abstract electrons from oxygen anions through Ag-O-Mn bridges, near which the oxygen molecules are possibly chemisorbed [53,62]. All the above factors are thought to be responsible for the high catalytic performance.

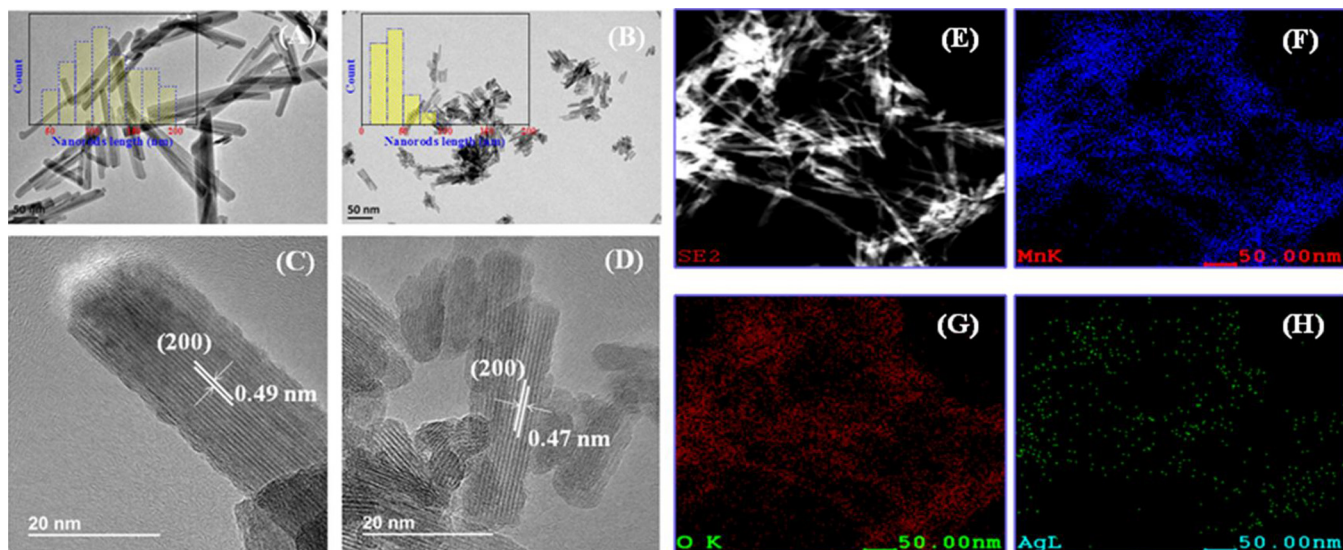


Fig. 5. TEM/HRTEM/Mapping images of the K/Ag-OMS-x catalysts, (A) TEM: K-OMS-2, (B) TEM: K/Ag-OMS-40, (C) HRTEM:K-OMS-2, (D) HRTEM:K/Ag-OMS-40, (E) HAADF-STEM image, (F) Mn-element mapping, (G) O-element mapping, (H) Ag-element mapping for K/Ag-OMS-40.

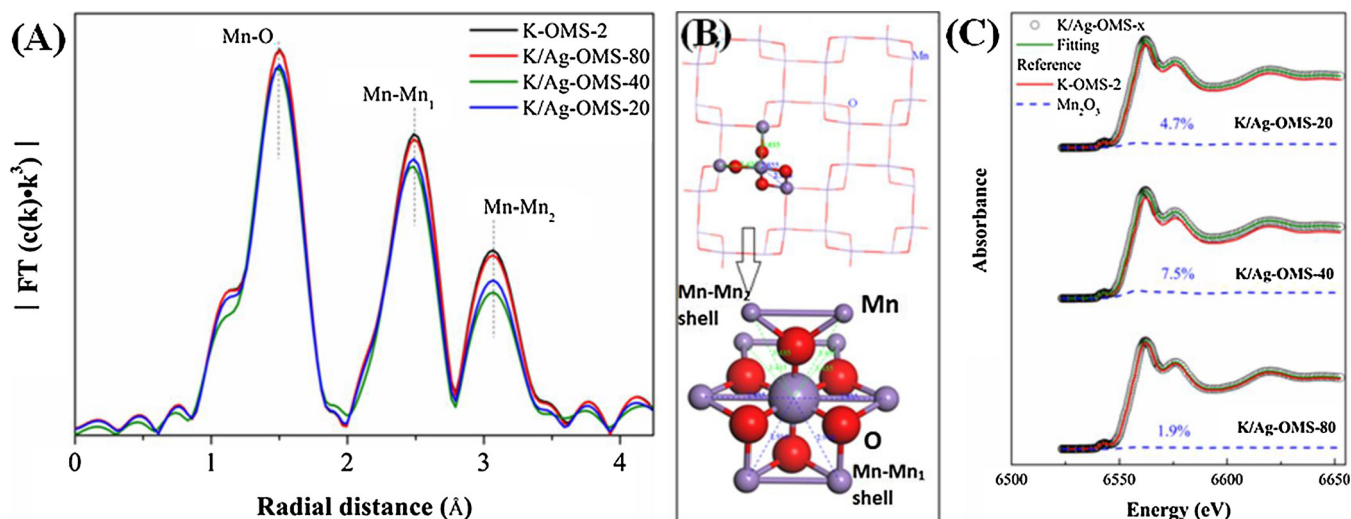


Fig. 6. EXAFS spectra of Mn K-edge in series of K/Ag-OMS-x catalysts (A), local structure model of K/Ag-OMS-x catalysts (B), and corresponding XANES spectra (C).

3.4. Activity of oxygen species

Labile surface oxygen species play a key role in catalytic oxidation over OMS-2 via the Mars–van Krevelen mechanism [27,39]. Since they usually take part in the redox reaction, H₂-TPR experiments were performed to investigate the reducibility of K/Ag-OMS-x. The final reduction product of MnO₂ could be MnO, with Mn₂O₃ and Mn₃O₄ as intermediates [28,35,43,55]. As shown in Fig. 7(A), the peak at 270 °C corresponds to the consumption of structural oxygen close to the surface, without decomposition of the material. The main reduction peak of K-OMS-2 can be basically decomposed into two equivalent peaks at around 304 and 324 °C respectively, indicating that the reduction route is MnO₂ to Mn₂O₃ and then to MnO.

After silver loading, all reduction peaks move toward lower temperature significantly. This is consistent with many other reports [40,51–55,62], affirming that silver incorporation could significantly improve the reducibility of OMS-2 [63–65]. The reduction of MnO₂ to Mn³⁺ and/or Mn²⁺ is enhanced via the spillover of hydrogen from silver atoms to manganese oxides [66,67]. Thus, a suitable synergistic interaction between Ag and MnO₂ favors the spillover of hydrogen and its subsequent reaction with MnO₂ [68]. The reducibility increases with the silver doping content and the general order can be listed as follows: K-OMS-2 < K/Ag-OMS-80 < K/Ag-OMS-40 < K/Ag-OMS-20. However, the H₂ consumption decreases with the rise in Ag content as follows: K-OMS-2 (13.61 mmol g⁻¹) > K/Ag-OMS-80 (13.48 mmol g⁻¹) > K/Ag-OMS-40 (13.37 mmol g⁻¹) > K/Ag-OMS-20 (12.98 mmol g⁻¹). On increasing the precursor silver doping, a new peak around 170 °C is observed for K/Ag-OMS-20, which could be ascribed to the reduction of a small amount of silver oxide species [68,69], implying that the silver species in K/Ag-OMS-20 were not dispersed as well as in K/Ag-OMS-40. Thus, a favorable synergistic interaction between Ag and K-OMS-2 should prevail in K/Ag-OMS-40 rather than K/Ag-OMS-20 in spite of both catalysts containing similar amounts of silver.

To further elucidate the activity of oxygen species in K/Ag-OMS-x

catalysts, a CO-TPD experiment was carried out. The kinetic diameter of CO is larger than the effective pore size of OMS-2, thus the internal silver sites are not accessible. Meanwhile, using the probe molecule CO can reveal the intrinsic activity of oxygen species and rule out interference from the H₂ spillover effect. As clearly shown in Fig. 7(B), CO₂ is produced by the surface reaction between adsorbed CO and the oxygen species of K/Ag-OMS-x catalysts. It is worth noting that no CO can be detected with ramping of temperature (Fig. S8). Two distinct CO₂ desorption peaks at around 150 and 450 °C were observed for the K/Ag-OMS-x nanorods. Desorption of CO₂ in the high temperature region around 450 °C could be attributed to the surface reaction of adsorbed CO with oxygen produced by the phase transformation of manganese oxides [47,48]. The desorption peak of CO₂ at 176 °C K-OMS-2 can be attributed to the oxidation reaction of CO on surface MnO₆ octahedral defect sites (K-O-Mn entities) [47].

As shown in Fig. 7(B), silver incorporation clearly provides new adsorption sites [47] (Ag-O-Mn entities) for CO, since a new desorption of CO₂ at lower temperature around 100 °C was found for silver-related samples. Moreover, desorption of CO₂ around 450 °C was observed for both K/Ag-OMS-40 and K/Ag-OMS-20. All of this confirms that the activity of surface oxygen species is truly enhanced via Ag-O-Mn bridges. In addition, the activity order of oxygen species derived from CO-TPD can be described as follows: K-OMS-2 < K/Ag-OMS-80 < K/Ag-OMS-20 < K/Ag-OMS-40, which is consistent with the catalytic performance. It is worthy of note that K/Ag-OMS-40 and K/Ag-OMS-20 have similar pore structures, surface areas and silver contents, but K/Ag-OMS-40 is much better than K/Ag-OMS-20 in abatement of benzene, as shown in Fig. 1(A). TEM images demonstrated that the nanorod size of K/Ag-OMS-40 is smaller than that of K/Ag-OMS-20, which leads to the formation of many more Mn octahedral defects, as illustrated in Fig. 6(A) and Table 2. H₂-TPR results indicated that a more favorable synergistic interaction between Ag and K-OMS-2 should prevail in K/Ag-OMS-40 than in K/Ag-OMS-20. CO-TPD experiments confirmed that K/Ag-OMS-40 possesses the most labile oxygen species owing to having the most abundant Mn octahedral defects and Mn³⁺/oxygen vacancies.

Table 2
Curve fitting results of Mn-K EXAFS for different K/Ag-OMS-x samples.

Sample	Shell	CN	R	σ^2 (Å)	R Factor ($\times 10^{-3}$ Å ²)	AOS	Mn ³⁺ (%)
K-OMS-2	(Mn-O, Mn-Mn ₁ , Mn-Mn ₂)	(5.44, 3.30, 3.28)	(1.90, 2.89, 3.44)	4.32	0.78	3.87	12.5
K/Ag-OMS-80	(Mn-O, Mn-Mn ₁ , Mn-Mn ₂)	(5.39, 3.22, 3.16)	(1.90, 2.89, 3.44)	4.28	0.79	3.75	14.4
K/Ag-OMS-40	(Mn-O, Mn-Mn ₁ , Mn-Mn ₂)	(5.38, 3.06, 2.73)	(1.90, 2.88, 3.44)	4.62	0.86	3.75	20.0
K/Ag-OMS-20	(Mn-O, Mn-Mn ₁ , Mn-Mn ₂)	(5.30, 3.07, 2.79)	(1.90, 2.88, 3.44)	4.45	0.87	3.75	17.2

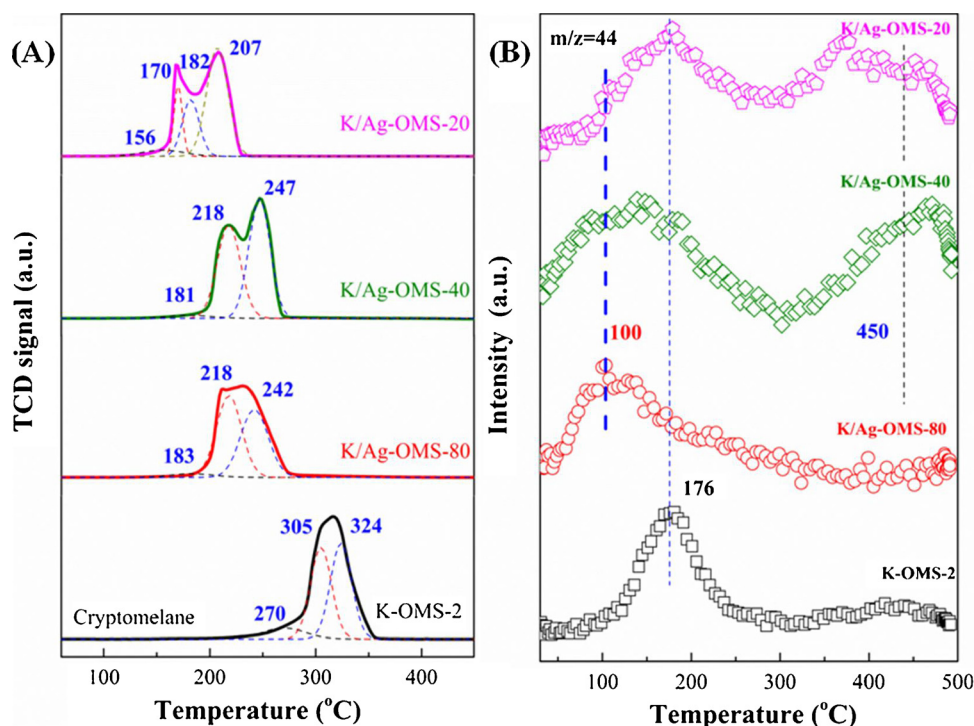


Fig. 7. $\text{H}_2\text{-TPR}$ profiles (A) and $\text{CO}\text{-TPD}$ profiles (B) of K-OMS-2 and K/Ag-OMS-x catalysts.

Thus, active oxygen species and Mn octahedral defects related to Ag-O-Mn bridges play more important roles in enhancing activity than the enhancement of the mesopore structure. That is the reason why K/Ag-OMS-40 exhibited the best activity in this study.

In summary, XRD, Raman and N_2 adsorption results indicated that the crystalline structure of cryptomelane is preserved after silver incorporation, but a significant increase in surface area and pore volume is observed via enhanced mesopores. ICP, XPS and elemental mapping results demonstrated that the K^+ in the tunnels of K-OMS-2 is partially replaced by highly dispersed Ag^+ . The replacement by the smaller radius Ag^+ ion results in the structure of K-OMS-2 becoming distorted. TEM and HRTEM results confirmed that the particle size of cryptomelane nanorods decreases after silver incorporation. The order of average nanorod size for K/Ag-OMS-x can be listed as follows: K-OMS-2 (173 nm) > K/Ag-OMS-80 (145 nm) > K/Ag-OMS-20 (72 nm) > K/Ag-OMS-40 (39 nm). As a consequence, K/Ag-OMS-40 has the lowest coordination number for the Mn-Mn coordination shell in the local structure, as depicted in the EXAFS results. This indicates that more abundant Mn octahedral defects are formed. Therefore, K/Ag-OMS-40 exhibits the most abundant Mn^{3+} and the highest number of labile oxygen species, as shown in XANES and TPD results respectively. All these results are consistent, demonstrating that K/Ag-OMS-40 is a promising candidate for eliminating VOCs.

4. Conclusions

K/Ag-OMS-x with different Ag exchange degrees was synthesized by a one-step hydrothermal method and tested in the catalytic oxidation of benzene vapor. Silver incorporation could enhance the benzene oxidation. The Ag^+ ions, the dominant form of Ag, replace K^+ in the tunnels of the cryptomelane structure and are well dispersed in the micropores. The exchange of K^+ by Ag^+ of smaller radius caused a significant decrease in the nanorod size of K-OMS-2, which significantly increased the surface area, number of Mn octahedral defects and amount of mixed-valence Mn (Mn^{3+} increment) in the catalyst. Moreover, silver exchange can form new Ag-O-Mn interaction entities to accelerate the charge transfer. The labile surface oxygen species

related to abundant Mn octahedral defects / Mn^{3+} content and Ag-O-Mn bridges played critical roles in the decomposition of VOCs. The K/Ag-OMS-40 catalyst exhibited the highest activity in terms of benzene combustion and good tolerance to chlorine poisoning, all of which make it a promising candidate for replacement of noble metal catalysts.

Acknowledgements

The work was supported by the National Key R&D Program of China (2016YFC0207104), the National Natural Science Foundation of China (51608504), and the Youth Innovation Promotion Association, CAS (2017064).

Appendix A. Supplementary data

Supplementary material related to this article can be found, in the online version, at doi:<https://doi.org/10.1016/j.apcatb.2018.08.006>.

References

- [1] Z. Hu, S. Qiu, Y. You, Y. Guo, Y.L. Guo, L. Wang, W.C. Zhan, G.Z. Lu, *Appl. Catal. B-Environ.* 225 (2018) 110–120.
- [2] S.I. Suarez-Vazquez, S. Gil, J.M. Garcia-Vargas, A. Cruz-Lopez, A. Giroir-Fendler, *Appl. Catal. B-Environ.* 223 (2018) 201–208.
- [3] Z. Ye, J.M. Giraudon, N. Nuns, P. Simon, N. De Geyter, R. Morent, J.F. Lamonié, *Appl. Catal. B-Environ.* 223 (2018) 154–166.
- [4] T. Montini, M. Melchionna, M. Monai, P. Fornasiero, *Chem. Rev.* 116 (2016) 5987–6041.
- [5] M.S. Kamal, S.A. Razzak, M.M. Hossain, *Atmos. Environ.* 140 (2016) 117–134.
- [6] L.F. Liotta, *Appl. Catal. B-Environ.* 100 (2010) 403–412.
- [7] S.H. Xie, Y.X. Liu, J.G. Deng, X.T. Zhao, J. Yang, K.F. Zhang, Z. Han, H. Arandiyan, H.X. Dai, *Appl. Catal. B-Environ.* 206 (2017) 221–232.
- [8] Z.Y. Jiang, C. He, N.F. Dummer, J.W. Shi, M.J. Tian, C.Y. Ma, Z.P. Hao, S.H. Taylor, M.D. Ma, Z.X. Shen, *Appl. Catal. B-Environ.* 226 (2018) 220–233.
- [9] R.S. Peng, S.J. Li, X.B. Sun, Q.M. Ren, L.M. Chen, M.L. Fu, J.L. Wu, D.Q. Ye, *Appl. Catal. B-Environ.* 220 (2018) 462–470.
- [10] N.N. Opembe, C.K. King'ondou, A.E. Espinal, C.H. Chen, E.K. Nyutu, V.M. Crisostomo, S.L. Suib, *J. Phys. Chem. C* 114 (2010) 14417–14426.
- [11] A. Iyer, J. Del-Pilar, C.K. King'ondou, E. Kissel, H.F. Garces, H. Huang, A.M. El-Sawy, P.K. Dutta, S.L. Suib, *J. Phys. Chem. C* 116 (2012) 6474–6483.
- [12] J.H. Li, R.H. Wang, J.M. Hao, *J. Phys. Chem. C* 114 (2010) 10544–10550.
- [13] R.H. Wang, J.H. Li, *Environ. Sci. Technol.* 44 (2010) 4282–4287.

- [14] V.D. Makwana, Y.C. Son, A.R. Howell, S.L. Suib, *J. Catal.* 210 (2002) 46–52.
- [15] N.N. Opembe, C. Guild, C. King'ondou, N.C. Nelson, I.I. Slowing, S.L. Suib, *Ind. Eng. Chem. Res.* 53 (2014) 19044–19051.
- [16] A.R. Gandhe, J.S. Rebello, J.L. Figueiredo, J.B. Fernandes, *Appl. Catal. B-Environ.* 72 (2007) 129–135.
- [17] L. Wang, C.B. Zhang, H. He, F.D. Liu, C.X. Wang, *J. Phys. Chem. C* 120 (2016) 6136–6144.
- [18] Y.S. Wu, R. Feng, C.J. Song, S.T. Xing, Y.Z. Gao, Z.C. Ma, *Catal. Today* 281 (2017) 500–506.
- [19] H. Sun, Z.G. Liu, S. Chen, X. Quan, *Chem. Eng. J.* 270 (2015) 58–65.
- [20] M.T.N. Dinh, T.M. Giraudon, A.M. Vandebroucke, R. Morent, N. De Geyter, J.F. Lamonié, *J. Hazard. Mater.* 314 (2016) 88–94.
- [21] A.M. El-Sawy, C.K. King'ondou, C.H. Kuo, D.A. Kriz, C.J. Guild, Y.T. Meng, S.J. Frueh, S. Dharmarathna, S.N. Ehrlich, S.L. Suib, *Chem. Mater.* 26 (2014) 5752–5760.
- [22] S. Dharmarathna, C.K. King'ondou, W. Pedrick, L. Pahalagedara, S.L. Suib, *Chem. Mater.* 24 (2012) 705–712.
- [23] H. Huang, S. Sithambaram, C.H. Chen, C.K. Kithongo, L.P. Xu, A. Iyer, H.F. Garces, S.L. Suib, *Chem. Mater.* 22 (2010) 3664–3669.
- [24] C. Calvert, R. Joesten, K. Ngala, J. Villegas, A. Morey, X.F. Shen, S.L. Suib, *Chem. Mater.* 20 (2008) 6382–6388.
- [25] X. Chen, Y.F. Shen, S.L. Suib, C.L. O'Young, *Chem. Mater.* 14 (2002) 940–948.
- [26] J.T. Hou, Y.Z. Li, M.Y. Mao, X.J. Zhao, Y.Z. Yue, *Nanoscale* 6 (2014) 15048–15058.
- [27] J.T. Hou, L.L. Liu, Y.Z. Li, M.Y. Mao, H.Q. Lv, X.J. Zhao, *Environ. Sci. Technol.* 47 (2013) 13730–13736.
- [28] M. Sun, W.P. Li, B.T. Zhang, G. Cheng, B. Lan, F. Ye, Y.Y. Zheng, X.L. Cheng, L. Yu, *Chem. Eng. J.* 331 (2018) 626–635.
- [29] W.N. Li, J.K. Yuan, S. Gomez-Mower, S. Sithambaram, S.L. Suib, *J. Phys. Chem. B* 110 (2006) 3066–3070.
- [30] C.K. King'ondou, N. Opembe, C.H. Chen, K. Ngala, H. Huang, A. Iyer, H.F. Garces, S.L. Suib, *Adv. Funct. Mater.* 21 (2011) 312–323.
- [31] H. Nur, F. Hayati, H. Hamdan, *Catal. Commun.* 8 (2007) 2007–2011.
- [32] L.A. Sun, Q.Q. Cao, B.Q. Hu, J.H. Li, J.M. Hao, G.H. Jing, X.F. Tang, *Appl. Catal. A-Gen.* 393 (2011) 323–330.
- [33] H. Yin, X.X. Dai, M.Q. Zhu, F.H. Li, X.H. Feng, F. Liu, J. Hazard. Mater. 296 (2015) 221–229.
- [34] Y.Z. Li, Z.Y. Fan, J.W. Shi, Z.Y. Liu, J.W. Zhou, W.F. Shangguan, *Catal. Today* 256 (2015) 178–185.
- [35] Y. Yang, J. Huang, S.Z. Zhang, S.W. Wang, S.B. Deng, B. Wang, G. Yu, *Appl. Catal. B-Environ.* 150 (2014) 167–178.
- [36] L.L. Zhang, J.J. Tu, L. Lyu, C. Hu, *Appl. Catal. B-Environ.* 181 (2016) 561–569.
- [37] V.P. Santos, O.S.G.P. Soares, J.J.W. Bakker, M.F.R. Pereira, J.J.M. Orfao, J. Gascon, F. Kapteijn, J.L. Figueiredo, *J. Catal.* 293 (2012) 165–174.
- [38] V.P. Santos, M.F.R. Pereira, J.J.M. Orfao, J.L. Figueiredo, *Appl. Catal. B-Environ.* 99 (2010) 353–363.
- [39] J. Luo, Q. Zhang, J. Garcia-Martinez, S.L. Suib, *J. Am. Chem. Soc.* 130 (2008) 3198–3207.
- [40] Y.X. Chen, Z.W. Huang, M.J. Zhou, Z. Ma, J.M. Chen, X.F. Tang, *Environ. Sci. Technol.* 51 (2017) 2304–2311.
- [41] Y. Lei, F. Mehmood, S. Lee, J. Greeley, B. Lee, S. Seifert, R.E. Winans, J.W. Elam, R.J. Meyer, P.C. Redfern, D. Teschner, R. Schlogl, M.J. Pellin, L.A. Curtiss, S. Vajda, *Science* 328 (2010) 224–228.
- [42] S.C. Kim, W.G. Shim, *Appl. Catal. B-Environ.* 92 (2009) 429–436.
- [43] J.Z. Ma, C.X. Wang, H. He, *Appl. Catal. B-Environ.* 201 (2017) 503–510.
- [44] C. Wang, J. Ma, F. Liu, H. He, R. Zhang, *J. Phys. Chem. C* 119 (2015) 23119–23126.
- [45] C.L. O'Young, R.A. Sawicki, S.L. Suib, *Microporous Mesoporous Mater.* 11 500–506.
- [46] Z.M. Wang, S. Tezuka, H. Kanoh, *Chem. Mater.* 13 (2001) 530–537.
- [47] J.L. Chen, X.F. Tang, J.L. Liu, E.S. Zhan, J. Li, X.M. Huang, W.J. Shen, *Chem. Mater.* 19 (2007) 4292–4299.
- [48] J.L. Chen, J. Li, H.J. Li, X.M. Huang, W.J. Shen, *Microporous Mesoporous Mater.* 116 (2008) 586–592.
- [49] J.T. Hou, Y.Z. Li, L.L. Liu, L. Ren, X.J. Zhao, *J. Mater. Chem. A Mater. Energy Sustain.* 1 (2013) 6736–6741.
- [50] Z.L. Wu, M.J. Li, J. Howe, H.M. Meyer, S.H. Overbury, *Langmuir* 26 (2010) 16595–16606.
- [51] G.D. Yadav, R.K. Mewada, *Chem. Eng. J.* 221 (2013) 500–511.
- [52] G.D. Yadav, R.V. Sharma, *Appl. Catal. B-Environ.* 147 (2014) 293–301.
- [53] M. Ozacar, A.S. Poyraz, H.C. Genuino, C.H. Kuo, Y.T. Meng, S.L. Suib, *Appl. Catal. A-Gen.* 462 (2013) 64–74.
- [54] G.D. Yadav, R.K. Mewada, *Chem. Eng. Res. Des.* 90 (2012) 86–97.
- [55] R.R. Hu, C.F. Yan, L.Y. Xie, Y. Cheng, D.Z. Wang, *Int. J. Hydrogen Energy* 36 (2011) 64–71.
- [56] A. Dyer, M. Pillinger, J. Newton, R. Harjula, T. Moller, S. Amin, *Chem. Mater.* 12 (2000) 3798–3804.
- [57] H.M. Galindo, Y. Carvajal, E. Njagi, R.A. Ristau, S.L. Suib, *Langmuir* 26 (2010) 13677–13683.
- [58] X.F. Shen, Y.S. Ding, J. Liu, Z.H. Han, J.I. Budnick, W.A. Hines, S.L. Suib, *J. Am. Chem. Soc.* 127 (2005) 6166–6167.
- [59] Y.G. Yin, W.Q. Xu, S.L. Suib, C.L. Oyoung, *Inorg. Chem.* 34 (1995) 4187–4193.
- [60] V.R. Galakhov, M. Demeter, S. Bartkowski, M. Neumann, N.A. Ovechkina, E.Z. Kurmaev, N.I. Logachevskaia, Y.M. Mukovskii, J. Mitchell, D.L. Ederer, *Phys. Rev. B* 65 (2002).
- [61] J.T. Hou, Y.Z. Li, M.Y. Mao, L. Ren, X.J. Zhao, *ACS Appl. Mater. Interfaces* 6 (2014) 14981–14987.
- [62] G.G. Xia, Y.G. Yin, W.S. Willis, J.Y. Wang, S.L. Suib, *J. Catal.* 185 (1999) 91–105.
- [63] W. Gac, G. Giecko, S. Pasieuna-Patkowska, T. Borowiecki, L. Kepinski, *Catal. Today* 137 (2008) 397–402.
- [64] W. Gac, *Appl. Catal. B-Environ.* 75 (2007) 107–117.
- [65] L.Y. Li, D.L. King, *Chem. Mater.* 17 (2005) 4335–4343.
- [66] S. Imamura, H. Sawada, K. Uemura, S. Ishida, *J. Catal.* 109 (1988) 198–205.
- [67] R. Xu, X. Wang, D.S. Wang, K.B. Zhou, Y.D. Li, *J. Catal.* 237 (2006) 426–430.
- [68] Q. Ye, J.S. Zhao, F.F. Huo, J. Wang, S.Y. Cheng, T.F. Kang, H.X. Dai, *Catal. Today* 175 (2011) 603–609.
- [69] J. Carno, M. Ferrandon, E. Bjornbom, S. Jaras, *Appl. Catal. A-Gen.* 155 (1997) 265–281.